Available online at www.sciencedirect.com
SCIENCE DIRECT®
Journal of Solid State Chemistry 177 (2004) 146–158
JOURNAL OF SOLID STATE CHEMISTRY
http://elsevier.com/locate/jssc

Magnetic properties of Ca-doped $SrRuO_3$ from full-potential calculations

R. Vidya,[a] P. Ravindran,[a,*] A. Kjekshus,[a] H. Fjellvåg,[a] and B.C. Hauback[b]

[a] *Department of Chemistry, University of Oslo, Box 1033, Blindern, N-0315, Oslo, Norway*
[b] *Institute for Energy Technology, P.O.Box 40, Kjeller, N-2007, Norway*

Received 18 March 2003; received in revised form 6 June 2003; accepted 3 July 2003

Abstract

We have carried out accurate generalized-gradient-corrected fully-relativistic full-potential calculations for $Sr_{1-x}Ca_xRuO_3$ ($x = 0$, 0.25, 0.5, 0.75, and 1) in para-, ferro-, and *A*-, *C*-, and *G*-type antiferromagnetic configurations. We have performed electronic structure calculations for the experimentally observed orthorhombic structure as well as the hypothetical cubic structure. Our results are analyzed with the help of total, site-, spin-, and orbital-projected density of states. The total-energy studies show that $CaRuO_3$ stabilizes in the *G*-type antiferromagnetic state. The octahedral tilting owing to the relatively small radius of Ca^{2+} leads to weak hybridization between Ru 4*d* and O 2*p*. This weak hybridization along with exchange splitting causes a pseudogap-like feature close to the Fermi level, which should stabilize *G*-type antiferromagnetic ordering in $CaRuO_3$. However, powder neutron diffraction data on $CaRuO_3$ taken at 8 and 298 K do not show any magnetic peaks, implying that $CaRuO_3$ exhibits a spin-glass-like state with dominant short-range antiferromagnetic interaction. The calculated magnetic ground state of $Sr_{1-x}Ca_xRuO_3$ is found to be consistent with the experimental findings. We have also calculated optical spectra as well as X-ray and ultra-violet photoemission spectra and Ru and O *K*-edge X-ray absorption spectra for *G*-type $CaRuO_3$ and found good agreement with available experimental spectra.

PACS: 71.; 71.20.-b; 75.50.Ee; 78.20.Ci

Keywords: Ruthenates; Magnetic properties; Spin-glass behavior; Excited properties

1. Introduction

Although oxides containing 4*d* and 5*d* metals have been known for a long time, their physical properties remain largely unexplored. However, since the discovery of superconductivity for some such oxides, this class of compounds have been studied intensively. The ruthenium-based perovskite $CaRuO_3$ is found to fulfill some of the requirements to an electrode material for solid-oxide fuel cells such as metallic conductivity and high chemical stability [1,2]. Moreover its high topotactic reduction/oxidation properties [3] make it interesting for catalysis purposes and its possible technological significance is enhanced by the observation of a strain induced metal–insulator transition in thin films [4]. $CaRuO_3$ epitaxial thin films have easy growth, good stability (with characteristics similar to those of single crystals), and only a small lattice mismatch with $YBa_2Cu_3O_{7-\delta}$ substrates. Hence, it is one of the most promising candidates for formation of epitaxial heterostructures with other perovskites, say, like electrodes for superconductor-to-normal-metal-to-superconductor junctions [5], field-effect transistors with oxide-superconductor channels, ferroelectrics [6], and magnetic multilayers. Particularly, the ferroelectric material $Bi_4Ti_3O_{12}$ has a low lattice mismatch with $CaRuO_3$ making it suitable as substrate for bottom electrodes of a ferroelectric random-access memory [7].

In order to exploit $CaRuO_3$ for technological applications, knowledge about its ground- and excited-state properties is essential. Although $SrRuO_3$ and $CaRuO_3$ are similar both structurally and chemically, their magnetic properties appear to be different. $SrRuO_3$ is a metallic conducting ferromagnet (F) [8,9], whereas the magnetic ground state of $CaRuO_3$ is still

*Corresponding author.
E-mail address: ponniah.ravindran@kjemi.uio.no (P. Ravindran).

0022-4596/$ - see front matter © 2003 Elsevier Inc. All rights reserved.
doi:10.1016/S0022-4596(03)00386-4

shrouded under controversy, but certainly not a clear-cut F state.

According to Callaghan et al. [8] $CaRuO_3$ follows Curie–Weiss law at high temperatures with negative Weiss constant (Θ). Longo et al. [9] were the first to "identify" a Néel temperature of 110 ± 10 K. The recent value for Θ is -160 K and the deviation from Curie–Weiss law classifies it as antiferromagnetic-like (AF) [10]. However, Mössbauer spectroscopic data collected [11] down to 4.2 K did not show magnetic splitting, and the absence of magnetic peaks in powder neutron diffraction (PND) diagrams [12] at 1.5 K appears to preclude the existence of long-range AF ordering in $CaRuO_3$. Martinez et al. [12] also report a clear departure from Curie–Weiss law behavior below 70 K which is interpreted as an indication of short-range AF correlations.

The low-temperature resistivity of $CaRuO_3$ shows [13] non-Fermi-liquid (NFL) behavior, a phenomenon theoretically expected near a quantum-critical point induced by a 0 K phase transition to an AF state. However, the measured magnetoresistance (MR) is positive at 5 K and low fields and becomes negative above ~ 40 K. In non-magnetic pure metals and alloys MR is generally positive and shows a quadratic dependence on the magnetic field. MR can be negative in magnetic materials as a result of suppression of the moment disorder by the magnetic field [14]. However, a transition to positive MR at low temperature while the magnetic susceptibility still increases is less expected. This suggests that changes in the behavior of the magnetic moments may occur.

Ab-initio calculations have so far not been able to resolve the contradictory experimental findings on the magnetic properties of $CaRuO_3$. Santi et al. [15] have performed extensive TBLMTO calculation on $CaRuO_3$ and obtained an F ground state, but without considering the possibility of AF states. They noted that the orthorhombic distortion favors cooperative magnetic states such as F, Ferri, and AF. Mazin and Singh [16] carried out full-potential LAPW calculation for the paramagnetic (P) and F states, and found that $CaRuO_3$ is in P state, but on the verge of F ordering. Their fixed-moment calculations show that the total energy of $CaRuO_3$ is nearly independent of magnetization up to 1 μ_B. Some of the present authors have earlier obtained the correct A-AF insulating ground state for $LaMnO_3$ [17], the C-AF state for $LaVO_3$ [18], and the G-AF state for $LaFeO_3$ [18]. This motivated us to probe the magnetic structure of $CaRuO_3$ by adopting the same procedure (accurate state-of-the-art relativistic-full-potential total-energy calculations), for all possible magnetic orderings with the interplane and intraplane ferro/AF exchange interactions. However, noncollinear magnetic configurations are not considered in the present study. We have done extensive electronic structure calculations on $Sr_{1-x}Ca_xRuO_3$ which may provide insight into why the isostructural $SrRuO_3$ and $CaRuO_3$ phases can take entirely different magnetic ground states. Since the magnetic ordering is contributed by the 4d electrons of Ru, relativistic effects such as spin–orbit (SO) coupling may be significant for this material. The reliability of the results can be improved by including inhomogeneity effects through the generalized-gradient approximation (GGA) [17]. Therefore, we have used a fully-relativistic full-potential method (with GGA) for the experimentally observed orthorhombic $GdFeO_3$-type (distorted perovskite) structure for $Sr_{1-x}Ca_xRuO_3$ as well as a postulated (hypothetical) ideal cubic perovskite structure for $CaRuO_3$. In an earlier study [19] the optical transition in $CaRuO_3$ is interpreted as a Mott–Hubbard transition, indicating that the compound is a strongly correlated material. However, a recent experimental optical property study [20] suggests that correlation effects are less significant. Hence a theoretical optical properties study has also been undertaken.

The rest of the paper is organized as follows. Structural aspects are described in Section 2.1, computational and experimental details are given in Sections 2.2 and 2.3, respectively. In Section 3 we discuss the magnetic ground state and electronic structure with the help of band structure, total, site-, and angular-momentum projected as well as orbital-projected density of states (DOS) curves. Excited state properties such as optical, ultra-violet photoemission (UPS), X-ray photoemission (XPS), and Ru and O K-edge X-ray absorption (XANE) spectra are considered in Section 4, and Section 5 summarizes the important findings.

2. Structural aspects, computational and experimental details

2.1. Crystal structure

$CaRuO_3$ stabilizes in the orthorhombic $GdFeO_3$-type structure comprising four formula units. The structural parameters obtained from PND and single-crystal X-ray diffraction data [3] are given in Table 1. The orthorhombic structure can be viewed as a highly distorted cubic perovskite structure with a quadrupled unit cell ($a_c\sqrt{2}$, a_c2, $a_c\sqrt{2}$ where a_c is the lattice parameter of the cubic perovskite). The relatively small size of Ca^{2+} leads to tilting of the octahedra in order to fill the space efficiently. The tilted octahedra form zig-zag chains through the corner-sharing linkage. The tolerance factor is a measure of tilting of the octahedra which is defined as $(R_A + R_O)/[\sqrt{2}(R_M + R_O)]$, where R_A, R_M, and R_O are the ionic radii for A, M, and O, respectively. The tolerance factor for $CaRuO_3$ is 0.88 which may be taken as another measure for the quite large distortion of this

particular atomic arrangement. The Ru–O–Ru bond angle is $\sim 150^\circ$ and the O–Ru–O angle $\sim 92^\circ$ at 293 K. The deviation of the Ru–O–Ru angle from 180° plays an important role for the ground-state properties of $CaRuO_3$. In order to evaluate the role of the orthorhombic distortion on electronic structure and ground-state properties, we have done calculations also for a hypothetical undistorted cubic perovskite structure. For the calculations on the ideal cubic variant we have used the experimental equilibrium volume of the orthorhombic structure. We found that it is important to use a consistent structure for different magnetic configurations to avoid the errors arising from the computational parameters. So, we have expressed the cubic structure into an equivalent orthorhombic structure with four formula units (i.e. $a = c = a_c\sqrt{2}$ and $b = 2a_c$). For the electronic structure calculations of $Sr_{1-x}Ca_xRuO_3$ we have used the structural description given in Ref. [21]. We have constructed a supercell consisting of four formula units and periodically replaced Sr by Ca. For example, $Sr_{0.25}Ca_{0.75}RuO_3$ contains one Sr and three Ca atoms in the supercell considered for calculations.

Four magnetic arrangements are possible depending on the interplane and intraplane couplings in perovskite oxides like $Sr_{1-x}Ca_xRuO_3$ (Fig. 1). (i) The ferromagnetic case where both inter- and intraplane couplings are F. (ii) With interplane AF coupling and intraplane F coupling the *A*-AF structure arises. (iii) The opposite arrangement with interplane F coupling and intraplane AF coupling is called *C*-AF structure. (iv) If both the inter- and intraplane couplings are AF the *G*-AF structure arises. A more detailed description of the different AF orderings is found in Ref. [17].

Table 1
Crystallographic data for $CaRuO_3$ derived by Rietveld analysis of PND data collected at 8 K

Parameter	PND; 8 K	SXD; 296 K
a (Å)	5.5311(2)	5.524(1)
b (Å)	7.6460(3)	7.649(2)
c (Å)	5.3408(2)	5.354(1)
Ca x	0.9443(4)	0.9448(4)
z	0.0125(7)	0.0139(2)
O(1) x	0.0218(4)	0.0258(6)
z	0.5939(4)	0.5920(6)
O(2) x	0.2020(3)	0.2021(5)
y	0.4514(2)	0.4518(3)
z	0.1980(3)	0.1973(4)

Space group *Pnma*; Ca and O(1) in 4*c*, Ru in 4*b*, and O(2) in 8*d*. Calculated standard deviations are given in parantheses. Single-crystal X-ray diffraction (SXD) data taken from Ref. [3] are included for comparison.

2.2. Computational details

The full-potential LMTO calculations [22] presented in this paper are all electron, and no shape approximation to the charge density or potential has been used. The base geometry in this computational method consists of muffin-tin and interstitial parts. The basis set is comprised of augmented linear muffin-tin orbitals [23]. Spherical-harmonic expansion of the charge density, potential, and basis functions were carried out up to $\ell = 6$. The calculations are based on the generalized-gradient-corrected density-functional theory as proposed by Perdew et al. [24].

The SO term is included directly in the Hamiltonian matrix elements for the part inside the muffin-tin spheres, hence for a spin-polarized case the size of the secular matrix is doubled. The present calculations made use of the so-called multi basis, which is important to obtain a reliable description of the higher lying unoccupied states, especially for the optical properties. The basis included 4*s*, 4*p*, and 3*d* states for Ca, 5*s*, 5*p*, and 4*d* states for Ru, and 2*s*, 2*p*, and 3*d* states for O. Earlier studies [16,15] have shown that the magnetic properties of ruthenates are very sensitive to the **k**-point density and hence the **k**-space integration for the total energetics was done using the special point method with 284 **k** points in the irreducible part of the first Brillouin zone (IBZ) for both the orthorhombic and cubic structure. The test calculations show that we have used well-converged **k**-point set. The experimental studies on single crystal show that the easy magnetization axis is along *c* for $CaRuO_3$ [25] as well as $Sr_{1-x}Ca_xRuO_3$ [26] and hence we have chosen [001] as the magnetization axis for all spin-polarized calculations. Using the derived self-consistent potentials, the imaginary part of

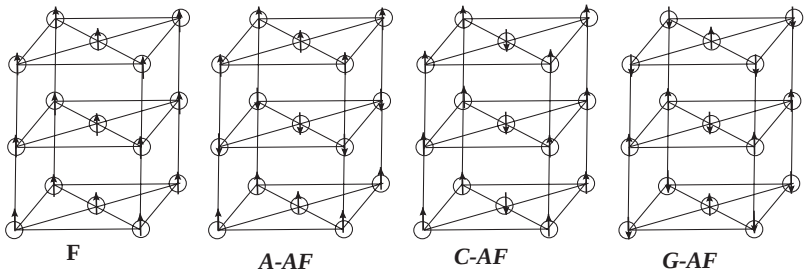

Fig. 1. The different types of magnetic ordering considered for the calculations of $Sr_{1-x}Ca_xRuO_3$.

the optical dielectric tensor and the band structure of $CaRuO_3$ were calculated for the *G*-AF state. The DOS was calculated using the linear tetrahedron technique. For the calculations of optical properties 584 **k** points are used in IBZ. The knowledge of both the real and imaginary parts of the dielectric tensor allows calculations of reflectivity, absorption coefficient, electron energy-loss spectrum (EELS), and refractive index. For this purpose we follow the definitions given in Ref. [27].

For metals, the intraband contribution to the optical dielectric tensor influences the lower-energy part of the spectra. This has been calculated using the unscreened plasma frequency obtained from Fermi surface integration according to the description in Ref. [27]. In order to calculate the unscreened plasma frequency and orbital-projected DOS (for *G*-AF state orthorhombic $CaRuO_3$) we have used the full-potential linearized augmented plane-wave (FPLAPW) method [28] in a scalar-relativistic version, without SO coupling. For these calculations we used atomic sphere radii (R_{MT}) of 2.1, 2.0, and 1.7 a.u. for Ca, Ru, and O, respectively. The charge density and the potentials are expanded into lattice harmonics up to $L = 6$ inside the spheres and into Fourier series in the interstitial region. The basis set included 4*s* valence states for Ca, 5*s*, 5*p*, and 4*d* for Ru, and 2*s* and 2*p* for O. Exchange and correlation are treated within GGA using the parameterization scheme of Perdew et al. [24]. To ensure convergence, 244 **k** points in IBZ were used. The results discussed in the following sections refer to the orthorhombic structure except where specifically mentioned as cubic.

2.3. Experimental

The synthesis of $CaRuO_3$ was performed by a standard solid-state reaction between well mixed fine powders of $CaCO_3$ (p.a., Merck; dried at 450°C for 1 day) and RuO_2 (99.9%, Aldric). The powder mixture was pelletized and calcined at 1200°C for 2 days in air. After cooling to room temperature the sample was carefully grinded, repelletized and the heat treatment was repeated.

The thus obtained sample was characterized by powder X-ray diffraction at 25°C with a Siemens D5000 diffractometer with reflection geometry using monochromatic Cu$K\alpha_1$ radiation from an incident beam Ge monochromator. The sample was mounted on a single crystal Si sample holder, the detector was a Brown PSD, and the diffraction pattern was collected over the 2θ range 10–90°. All reflections were indexed in accordance with the structural data for $CaRuO_3$ and the sample was accordingly considered phase pure.

The sample was also subjected to thermogravimetric analysis with a Perkin-Elmer TGA7 system in air. A silica-glass container was used as sample holder. The heating rate was 10°C min^{-1} and the sample size was ~50 mg. The heating sequence (temperature in °C was): 25 → 1200 → 500 (held for 5 h) → 25. This heat treatment exposed no mass changes which could have been an indication of variation in oxygen stoichiometry.

High-resolution PND data (Fig. 2) for $CaRuO_3$ were collected at 8 and 298 K with the PUS two-axis diffractometer [$\lambda = 1.555$ Å, focussing Ge(511) monochromator] accommodated at the JEEP II reactor,

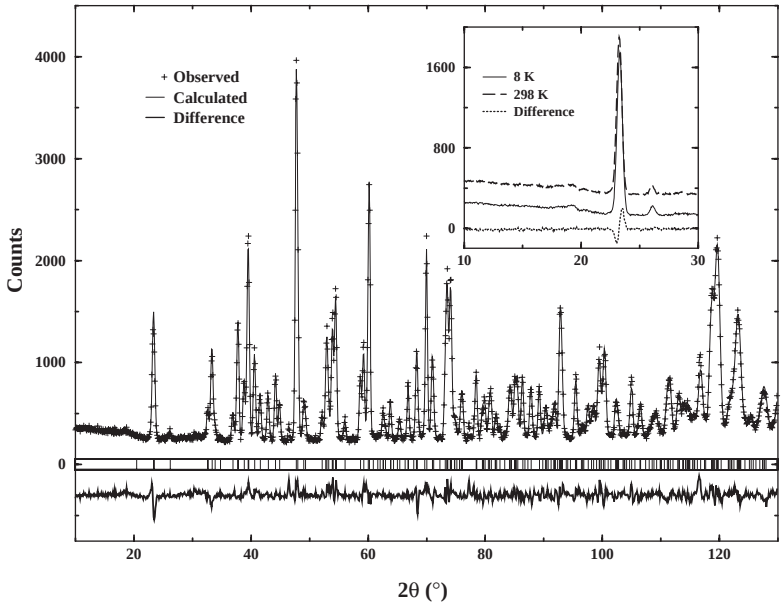

Fig. 2. Observed (crosses) and calculated (solid line) PND intensity profiles for $CaRuO_3$ at 8 K. The vertical lines indicate the positions for Bragg reflections and the lower part of figure shows the difference plot, I(obs)−I(calc). Inset shows enlarged portion of the low-angle parts of diagrams taken at 8 and 98 K with higher resolution than for the structure determination.

Kjeller, Norway. The sample was contained in a cylindrical vanadium holder with 3 mm inner diameter. A Displex cooler was used at 8 K. The diffraction pattern was registered by means of two detector banks, each covering 20° in 2θ and each containing a stack of seven position sensitive detectors [29]. The General Structure Analysis System ((GSAS) [30]) was used for Rietveld refinements of the PND data. Nuclear scattering lengths were taken from the GSAS library. The background was modelled as a cosine Fourier series polynomial (12 terms). The peak shape was modelled by a pseudo-Voight function. The PND data used for the least-squares refinements included 2400 data points (2θ range 10–30°, step length 0.05°).

3. Results and discussion

3.1. Magnetic properties

The total energy for different magnetic configurations obtained from our calculations are given in Table 2. From this table, it is obvious that $CaRuO_3$ should stabilize in the *G*-AF state. The FPLMTO method used in these calculations is capable of resolving total energy differences of the order of μRy [31] and we conclude that the energy differences of the order of meV between different magnetic configurations are significant. We are gaining around 26 meV when we include *G*-AF in the calculations. Owing to the small exchange splitting in this material, the energy difference between the different magnetic configurations is small compared to isostructural $LaMnO_3$ [17].

Table 3 shows that the Ru magnetic moment of the *G*-AF state is larger than that of F state for orthorhombic $CaRuO_3$. The magnetic moments at the O(1) and O(2) sites in the direction of Ru are 0.000 and 0.005 μ_B, respectively, in the *G*-AF state, and in the F state, 0.034 and 0.032 μ_B, respectively. The enhanced moment at the Ru site in the F state induces more moment in the O site than that in the AF state. In order to check whether the octahedral tilting plays a role in stabilizing *G*-AF, we have done similar calculations for the hypothetical cubic perovskite structure of $CaRuO_3$, in all five magnetic configurations. The results show that one loses a large amount of total energy in the cubic case indicating that the energetics associated with the octahedral tilting are higher than the magnetic energy. Interestingly, the

Table 2
Total energies (relative to the lowest energy state in meV/f.u.) of $Sr_{1-x}Ca_xRuO_3$ for the orthorhombic phase in P, F, *A*-, *C*-, and *G*-AF states using FLMTO with GGA and SO coupling

Compound	P	F	*A*-AF	*C*-AF	*G*-AF
$SrRuO_3$	89	0	48	63	75
$Sr_{0.75}Ca_{0.25}RuO_3$	69	0	57	47	59
$Sr_{0.5}Ca_{0.5}RuO_3$	111	0	57	84	22
$Sr_{0.25}Ca_{0.75}RuO_3$	27	0	19	4	0.79
$CaRuO_3$	26	19.8	6	4	0
$CaRuO_3$ (GGA without SO)	38	0	9	10	7
$CaRuO_3$ (cubic)	1307	1249	1292	1299	1303

Data for the hypothetical cubic phase of $CaRuO_3$ are included for comparison. For the cubic phase the total energies are given relative to orthorhombic *G*-AF phase.

Table 3
Calculated magnetic moment (in μ_B/Ru atom) for $Sr_{1-x}Ca_xRuO_3$ in F and *A*-, *C*-, and *G*-AF state

Compound	F	*A*-AF	*C*-AF	*G*-AF	Total	Literature
$SrRuO_3$	0.92	0.67	0.57	0.52	1.43	0.79[1], 0.85[2]
$Sr_{0.75}Ca_{0.25}RuO_3$	0.78	0.33	0.50	0.33	1.20	0.67[1]
$Sr_{0.5}Ca_{0.5}RuO_3$	0.99	0.78	0.66	0.66	1.51	0.35[1]
$Sr_{0.25}Ca_{0.75}RuO_3$	0.62 (0.38)[3]	0.30	0.53	0.53	0.77	0.01
$CaRuO_3$	0.28	0.53	0.54	0.59	0.44	1.93[4], 1.8[5]
$CaRuO_3$ (GGA without SO)	0.65	0.60	0.60	0.62	1.00	—
$CaRuO_3$ (cubic)	0.76	0.43	0.40	0.37	1.20	—

Total refers to the total magnetic moment per formula unit in the F state. The magnetic moments are calculated with FLMTO, GGA, and SO coupling. Data for the hypothetical cubic phase of $CaRuO_3$ are included for comparison.

[1] From TB-LMTO-ASA calculations. Ref. [15].

[2] From experiment, Ref. [32].

[3] Ru atoms have different magnetic moments depending upon the nearest-neighbors, see text.

[4] Measured spontaneous magnetic moment per Ru atom, Ref. [33].

[5] From magnetization measurement, Ref. [8].

ground state of the hypothetical cubic phase is F indicating the presence of strong magneto-elastic coupling in this material. In order to understand the role of the SO coupling on the magnetic properties of ruthenates we have made total-energy studies for all five magnetic configurations of $CaRuO_3$ neglecting the SO coupling. For orthorhombic $CaRuO_3$ without inclusion of SO coupling, the F state represents the lowest energy configuration with 7 meV/f.u. lower energy than the *G*-AF state (Table 2). This strongly suggests that the SO coupling plays an important role in deciding the magnetic properties of ruthenates.

The establishment of *G*-AF as the most probable ground state motivated a redetermination of $CaRuO_3$ by the PND technique. However, a very careful examination of the 8 and 298 K PND diagrams (Fig. 2) [32,35] showed no sign of cooperative long-range AF ordering at low temperatures (in agreement with Refs. [11,12]). Hence, the exchange interactions in $CaRuO_3$ must be short ranged. Recent magnetization measurements [25] show irreversibility in the zero-field-cooled and field-cooled characteristics indicating spin-glass (SG) behavior. Compared with the energy difference between the *G*-AF and F states of $SrRuO_3$ (Table 2), the energy differences between the magnetic states of $CaRuO_3$ are small indicating that SG is a very likely state for $CaRuO_3$. Some of the common characteristics of SG states are: (i) Existence of a local moment. (ii) Absence of long-range magnetic order. (iii) Higher susceptibility with field-cooled than zero-field cooled treatment. $CaRuO_3$ is found to possess all these characteristics (present results and Ref. [25]). In addition, as a result of the small energy difference between the magnetic states of $CaRuO_3$, the SG behavior of this material may also be facilitated by small perturbations from, say, oxygen nonstoichiometry (MnO exhibits AF ordering, $MnO_{1.01}$ shows SG behavior [34]), impurities (SG behavior is reported in Sn- [35] and Rh-doped [36] $CaRuO_3$), etc. It may also be recalled that SG behavior has been observed in La_2MnRuO_6 [37].

The main reason for SG behavior (magnetic frustration) of $CaRuO_3$ is the delicate balance between the F and (various) AF nearest-neighbor interactions. The energy difference between *A*-, *C*-, and *G*-AF states are small. Hence a competition among different AF interactions leads to a situation where no single configuration of the moments is uniquely favored by all interactions. This situation is nothing but magnetic frustration. A real SG material is expected to have both long- and short-range terms in the Hamiltonian [38]. Our calculations suggest that AF terms dominate the cooperative magnetic states of $CaRuO_3$, but PND data does not reveal any long-range magnetic ordering, leading to the belief that the AF interactions should be short-range. So we conclude that $CaRuO_3$ exhibits SG-like behavior with short-range *G*-AF ordering. This observation is consistent with experimental results such as the susceptibility measurements [10] which suggest a Weiss temperature of around 160 K and deviations from Curie–Weiss law which indicate short-range AF interactions (because no long range AF ordering is seen in PND).

We have performed similar magnetic calculations for the series $Sr_{1-x}Ca_xRuO_3$ ($x = 0$, 0.25, 0.5, 0.75, and 1). The calculated total energy and magnetic moments are given and compared with available literature data in Tables 2 and 3. From the magnetic phase diagram data in Ref. [39] it is clear that the AF-to-F transition takes place around $x = 0.75$ (from experimental studies) and $x = 0.724$ from our theoretical study. This provides additional support for the proposed dominant AF interactions in $CaRuO_3$.

According to Goodenough [40] a change between F and AF states may be expected when $\mu_F \approx \mu_{AF}$, the stable magnetic phase being the one that has highest magnetic moment. Our calculated results are consistent with this viewpoint in that the magnetic moments are found to be larger for the stable magnetic configuration in $Sr_{1-x}Ca_xRuO_3$ (see Table 2). Ru obtains two different moments (0.62 and 0.38 μ_B/Ru atom) for the F ground state of $Sr_{0.25}Ca_{0.75}RuO_3$, (Ru with two Ca atoms at close distance having the higher moment, the other value refers to Ru with one Sr and one Ca at close distance). No such distinction between Ru moments was found for the compositions $Sr_{0.5}Ca_{0.5}RuO_3$ and $Sr_{0.75}Ca_{0.25}RuO_3$. The special situation for $Sr_{0.25}Ca_{0.75}RuO_3$ being clearly related to the closeness of this composition to the change-over between dominant F and AF interaction (see above).

The calculated magnetic moment at the Ru site for $SrRuO_3$ is 0.92 μ_B/Ru atom in good agreement with 0.85 μ_B/Ru atom obtained from magnetization measurements [8]. As the Ca content decreases in $Sr_{1-x}Ca_xRuO_3$, the F interaction becomes stronger [21] (there are only insignificant changes in the Ru–O bond distance), following the decrease in the Ru–O–Ru bond angle from 164° to 150°. It is the thus weakened covalent Ru–O interaction (compared to that in $SrRuO_3$) which makes the *G*-AF state more stable than the F state. The crystal orbital Hamiltonian population (COHP) gives a quantitative measure of the bonding interaction between two constituents of a compound [41,42]. The (calculated) integrated COHP for the Ru–O covalent bond in $CaRuO_3$ and $SrRuO_3$ are 0.22 and 0.23 Ry per unit cell, respectively. Therefore we conclude that the increased tilting of the RuO_6 octahedra resulting from the smaller size of Ca^{2+} plays an important role in stabilizing an AF situation in the SG state of Ca-rich $Sr_{1-x}Ca_xRuO_3$. It is to be noted that a the sister-compounds Ca_2RuO_4 [43] and $Ca_3Ru_2O_7$ [26] take AF arrangements at low temperature. We have also made F state calculations for the closely related

compounds $BaRuO_3$ [11] and $LaRuO_3$ [10] and found no spontaneous magnetism in these materials (see also Refs. [10,11,44]). So, long-range magnetic ordering or SG-like behavior is not a general feature for ruthenates.

3.2. Band structure

Since we have established that the short-range interaction is of the *G*-AF type in orthorhombic $CaRuO_3$, we here present the electronic structure for this phase. The experimentally determined [44] single-crystal electrical resistivity classifies $CaRuO_3$ as a poor metallic conductor ($\rho = 3.7 \times 10^{-3}\ \Omega\ cm^{-1}$ at room temperature with a positive temperature coefficient). Fig. 3 shows that a finite number of bands cross the Fermi level (E_F), implying consistency between experiment and theory. For simplicity only bands in the energy region −8 to 8 eV are shown in Fig. 3. As Ca appears to be in a completely ionized state, only Ru and O have a predominant presence in the valence band (VB). Around −8 eV, Ru-5*s* and O-2*p* electrons show some presence. In the energy from −8 to −2.5 eV both Ru 4*d* and O 2*p* are dominant and they are hybridized. The bands in the energy range from −2 to 0.75 eV mainly originate from Ru 4*d* with small contributions from O 2*p*. From the orbital-projected DOS, it is found that the bands at E_F have predominant Ru-4*d* (t_{2g}-like) character. The well-dispersed bands from 1.5 to 5 eV in the conduction band (CB) stem mainly from Ca-4*s* and Ru-4*d* (e_g-*like*) electrons. Above 5 eV the bands have mixed character which makes it quite difficult to establish their origins.

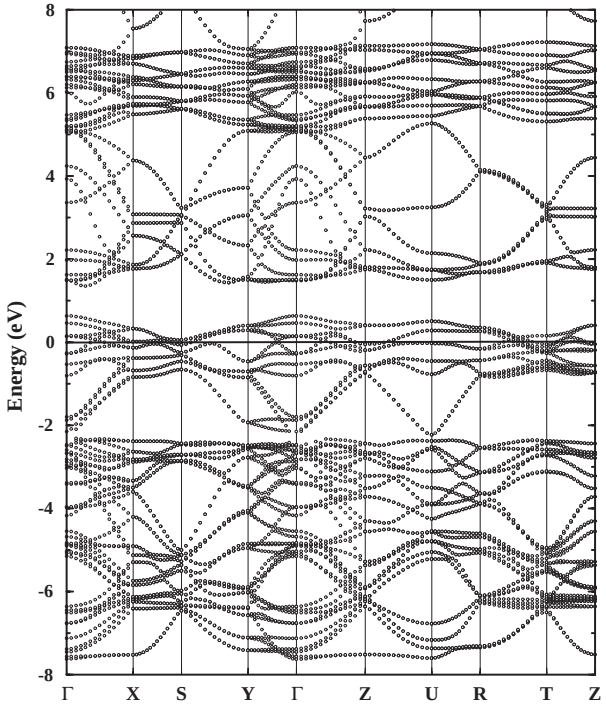

Fig. 3. Band structure of orthorhombic $CaRuO_3$ in *G*-type AF state. The solid horizontal line denotes the Fermi level.

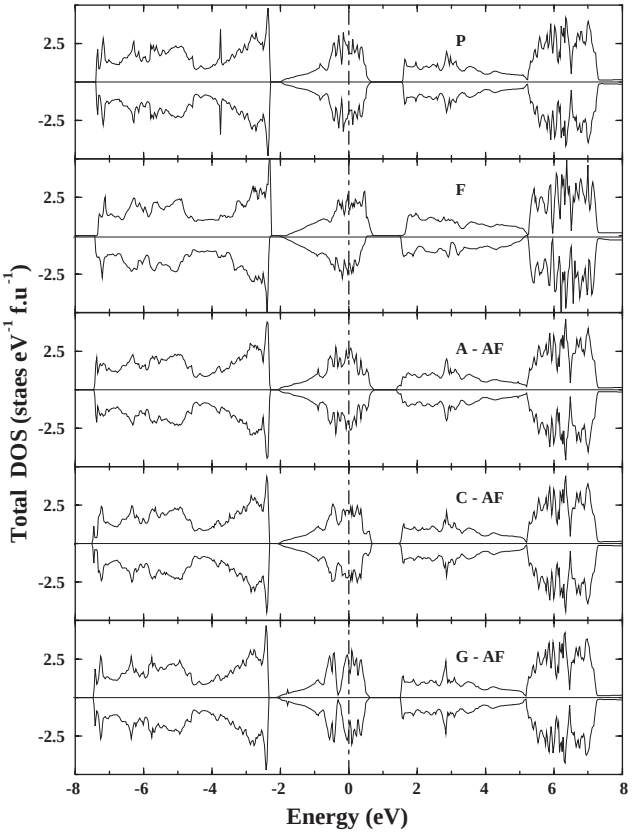

Fig. 4. Total DOS of orthorhombic $CaRuO_3$ in different magnetic configurations.

3.3. DOS

The total DOS for $CaRuO_3$ in all considered magnetic configurations are shown in Fig. 4. Although these DOS profiles appear to be similar with respect to energy, they show appreciable topological differences. In all five cases, DOS is spread out from −7.75 to −2.5 eV in VB and a small but finite gap of ∼0.25 eV opens up around the latter energy region. An interesting aspect of DOS for the *C*- and *G*-AF states is the occurrence of a valley-like feature (pseudogap-like feature, called PG-like, hereafter) in the vicinity of E_F (around −0.31 eV). It should be noted that similar pseudogap feature is observed [45] experimentally for the closely related phase $BaRuO_3$. As the PG-like feature is also favorable for stability, one should expect orthorhombic $CaRuO_3$ to stabilize in a *C*- or *G*-AF magnetic structure. A pseudogap is known to occur due to covalent hybridization, exchange splitting, charge transfer, and/or *d* resonance [46]. If the valence electrons of the constituents of a compound exist in the same energy region, their wave functions will mix strongly with each other and this covalent hybridization increases the bond

strength by pulling the electrons concerned to lower energy and thereby produce a pseudogap. In the present case, apart from the Ru-4*d* and O-2*p* hybridization which splits the t_{2g}-like electrons, the exchange splitting by the *C*/*G*-AF ordering causes the PG-like feature. Moreover, the PG-like feature is predominant in the *G*-AF phase indicating that the nearest neighbor AF interaction plays an important role in its creation. The presence of the PG-like feature will contribute to the total energy as a gain in band energy. Our calculations show that the gain in the band energy is 66 meV for *G*-AF compared with the F state. This finding clearly shows that the PG-like feature is responsible for the stabilization of the *G*-AF phase over the other phases considered.

However, a closer investigation of the DOS profile for the *G*-AF state shows that the PG-like feature is not exactly at E_F (which would have enhanced the stability) and the location of E_F close to a sharp peak-like feature may in fact, induce a degree of instability to the phase. This provides an additional hint as to why long-range antiferromagnetic ordering is lacking in $CaRuO_3$. Oxygen nonstoichiometry and hole doping can bring E_F towards the PG-like feature and stabilize the *G*-AF-type ordering. This may explain why long-range AF ordering has been reported for some $CaRuO_3$ samples [9]; Na-doped [32] and 1%-Fe-doped $CaRuO_3$ (Mössbauer spectroscopy at 4.1 K [25]). The calculated DOS at E_F $[N(E_F)]$ for the *G*-AF phase is 58.4 states/(Ry f.u.) and this yields a electronic specific-heat coefficient of 10.13 mJ/mol K^2 without including electron-phonon mass-enhancement effect and spin fluctuations. The experimental electronic specific-heat [25] at low temperature for a single crystal is 77.5 mJ/mol K^2.

The total DOS of cubic $CaRuO_3$ for all five magnetic configurations is shown in Fig. 5. Substantial differences in the DOS profiles are seen between the cubic and orthorhombic phases (Fig. 4, 5). Notably the small band gap of ~0.25 eV around −2 eV and the sharp peak-like feature at −2.25 eV are absent for the cubic phases. However, more significantly, E_F falls on a peak for all AF states of the cubic variant (an exchange splitting of ~0.5 eV is seen for the F state). As the location of E_F at a peak in DOS is unfavorable for stability, $CaRuO_3$ does not take the cubic arrangement. The total energy for all magnetic configurations of the cubic phase is moreover higher than those of the orthorhombic phase (see Table 2). Another interesting aspect is the absence of the PG-like feature for the cubic phase which implies that the occurrence of the feature in the orthorhombic AF phases is mainly due to octahedral tilting and further deepened by the exchange splitting. The exchange splitting of Ru 4*d* in *G*-AF orthorhombic $CaRuO_3$ is ~0.38 eV compared with 3.34 eV for Mn 3*d* in *A*-AF $LaMnO_3$ [17]. This is because, owing to the broader nature of 4*d* compared with 3*d* states, the

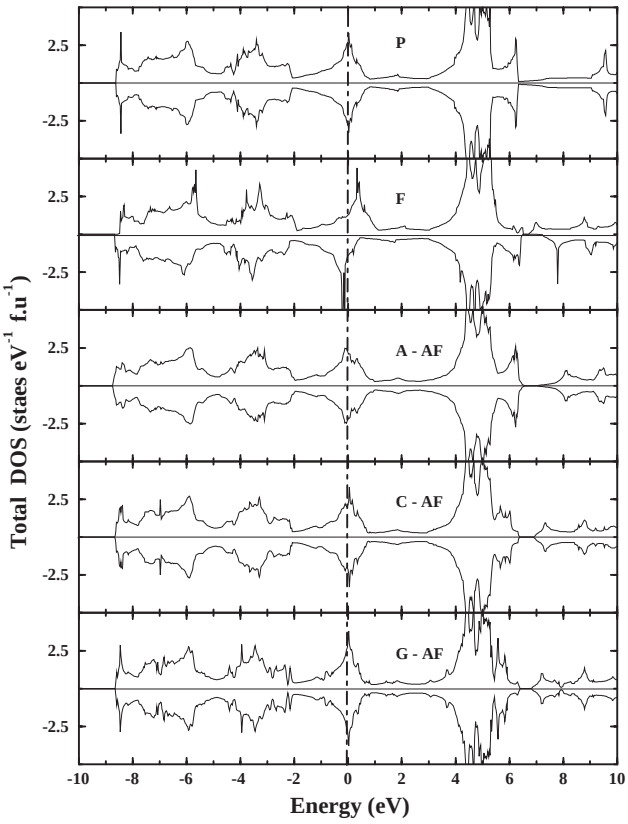

Fig. 5. Total DOS of hypothetical cubic $CaRuO_3$ in different magnetic configurations.

magnetic moments of 4*d* elements (0.58 μ_B for Ru in *G*-AF $CaRuO_3$) is smaller than those of 3*d* elements (3.43 μ_B for Mn in *A*-AF $LaMnO_3$ [17]). On going from *A*- to *G*-AF orthorhombic $CaRuO_3$ the magnetic moment at the Ru site increases. Our calculated value for the exchange energy of $CaRuO_3$ is comparable with that for the closely related $SrRuO_3$ (0.5 and 0.65 eV from experimental [47] and theoretical [48] studies, respectively). Further, due to the tilting of the RuO_6 octahedra, the Ru–O hybridization interaction in $CaRuO_3$ is smaller than that in $SrRuO_3$ and hence the Ru-4*d* electrons are more localized and favor AF ordering for $CaRuO_3$.

More insight into the electronic structure can be obtained by looking at the site-, spin-, and angular-momentum-projected DOS (Fig. 6). Ca-4*s* and -4*p* electrons have only feeble presence in VB, the indication that Ca is in a completely ionized state, donating almost all its electrons to O 2*p*. In the lowest energy range (−20 to −17 eV) the DOS is dominated by O-2*s* electrons with small contribution from Ru-5*s* and -5*p* electrons. The predominant presence of Ru-4*d* and O-2*p* states between −7.5 and E_F implies hybridization between these electrons. The PG-like feature is present both in Ru 4*d* and O 2*p*, indicating that the *d*–*p* hybridization is one of the reasons for the occurrence of the PG-like feature. The two O positions have somewhat different DOS. The

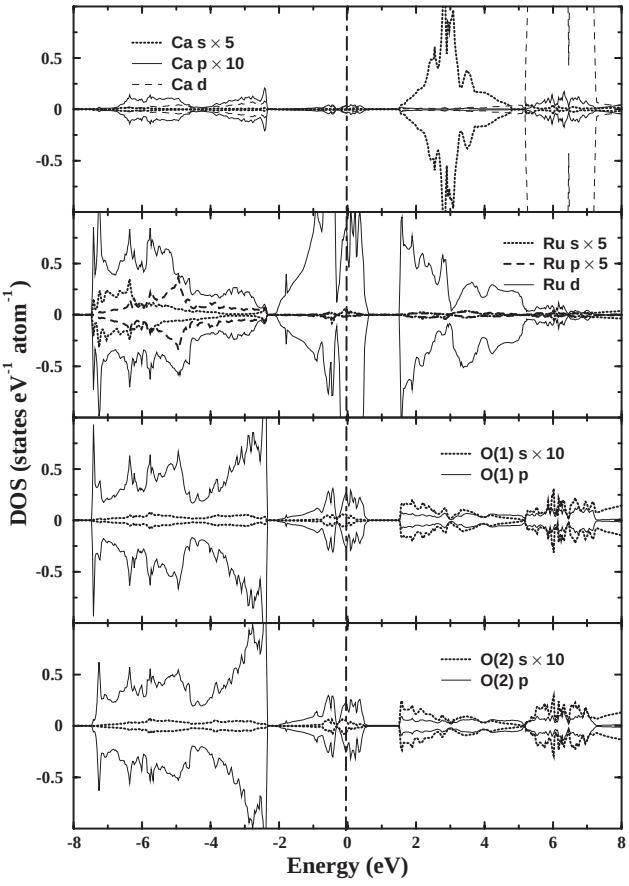

Fig. 6. Site- spin- and angular-momentum-projected DOS for orthorhombic G-AF $CaRuO_3$ obtained from FPLMTO method.

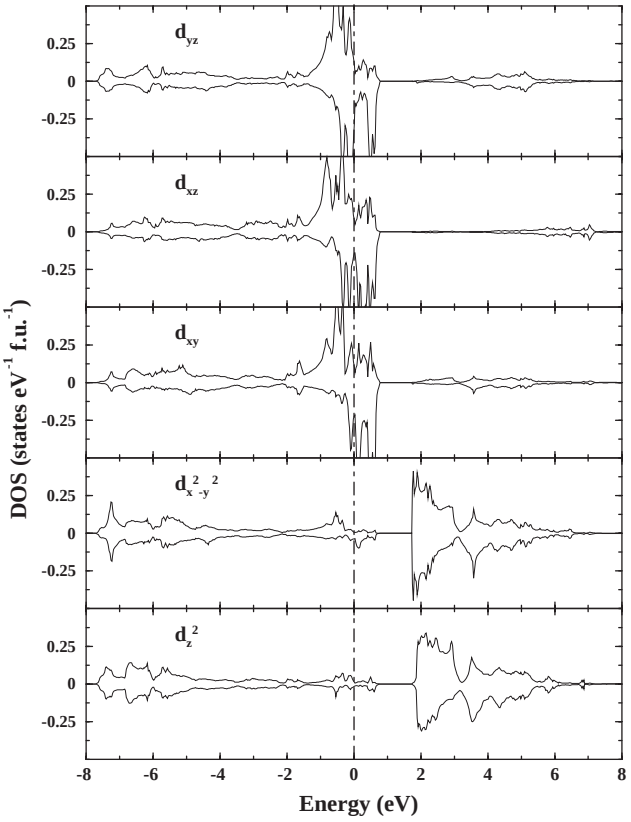

Fig. 7. Orbital-projected DOS of Ru 4d for orthorhombic G-AF $CaRuO_3$ from FPLAPW method.

sharp peak around −7.8 eV is not so well-defined for O(2) as for O(1), indicating formation of p–d σ bonding along c.

Earlier studies show that [1] the direct Ru–Ru interaction has been ruled out by the larger Ru–Ru separation (5.60 Å) compared with, say, 2.65 Å in metallic Ru. However, our calculations show that more than 50% of the DOS at E_F (4.29 states eV^{-1} f.u.$^{-1}$) is contributed by the Ru-4d electrons. This indicates that the Ru-4d electrons participate appreciably in the metallic conduction. Compared with $CaRuO_3$, the magnetic moment at the O site in $SrRuO_3$ is very large [16] (some 40% of the total moment resides at the O site) and this distinction is due to the tilting of octahedra in $CaRuO_3$ and also the AF ordering which yields lower induced moments at the neighbors.

In order to obtain more insight about the Ru-4d states in $CaRuO_3$, we show the orbital-projected DOS in Fig. 7. In the hypothetical cubic crystal structure, the d orbitals split into doubly-degenerate e_g-like (d_{z^2} and $d_{x^2-y^2}$; we call it e_g; usually close to E_F) and triply-degenerate t_{2g}-like (d_{xy}, d_{xz}, and d_{yz}; we call it t_{2g}; usually well-localized) states. However, owing to the large tilting of the octahedra in orthorhombic $CaRuO_3$, the t_{2g} orbitals lie close to E_F while the e_g orbitals are spread out over a wide energy range in VB and CB. From Fig. 7 it is clear that t_{2g}-electrons mainly participates in the magnetism of $CaRuO_3$. The crystal-field-splitting energy (10Dq) obtained from our orbital-projected DOS is around 2.5 eV and this value is comparable with 3.0 eV obtained from optical measurements [20] and in agreement with 2.5 eV obtained for $SrRuO_3$ by Singh [48] from LAPW calculations. The fact that 10Dq for $CaRuO_3$ is larger than that calculated for A-AF $LaMnO_3$ ($\sim$1.2 eV [17]) reflects the extended nature of 4d orbitals compared with 3d orbitals. Also, the strong orthorhombic distortion along with the anisotropic Coulomb potential due to the surrounding oxygen ions could influence the Ru-4d orbitals appreciably. The large contribution from t_{2g} over e_g electrons at E_F indicates that the t_{2g} electrons are mainly responsible for not only the magnetic properties but also for transport properties. (In $LaMnO_3$ the t_{2g} electrons contribute to magnetism and the e_g electrons to the transport properties.) Another notable aspect of the DOS profiles is that the PG-like feature is present for all t_{2g} orbitals. Owing to the tilting of octahedra, the t_{2g} orbitals participate more than the e_g orbitals in the covalent bonding with O 2p, and hence each of them has different DOS profiles depending upon their orientation whereas the topology of the DOS curves for the e_g

electrons do not differ much and these electrons do not participate much in the magnetism of $CaRuO_3$.

From the optical properties study [19] it has been suggested that Ru ions are in a low spin $t_{2g}^4 e_g^0$ configuration. In this case the e_g states would be empty and the t_{2g} states would have around 4 electrons. Our orbital-projected DOS (Fig. 7) shows that around 1.3 electrons are present in the e_g states and their contribution to the magnetism is negligibly small ($\sim 0.03\ \mu_B$/Ru atom). Our calculation shows that around 3.3 electrons are present in the t_{2g} states and that they are responsible for the magnetism ($\sim 0.55\ \mu_B$/Ru atom). So, the Ru ions are clearly not in a low-spin state in $CaRuO_3$ and the relatively small moment in this compound originates from the smaller exchange splitting which in turn reflects the extended nature of the 4*d* orbitals.

4. Excited state properties

4.1. Optical properties

A deeper understanding of electronic structures can be obtained by studying optical spectra which not only give information about the occupied and unoccupied states, but also about the character of bands. Therefore we have calculated optical properties for orthorhombic *G*-AF $CaRuO_3$ (Fig. 8) and compared them with available experimental data by [20,47,49–53]. Since $CaRuO_3$ is a metallic conductor, it is important to take into account the intraband contributions to the optical transitions in addition to the interband transitions. We have made use of the FPLAPW (WIEN97) code [28] for this purpose. The calculated unscreened plasma frequency (ω_p) along the crystallographic directions *a* (0.86 eV) and *b* (0.83 eV) are almost the same. However, ω_p along *c* takes a somewhat smaller value (0.66 eV) indicating some anisotropy in the transport properties. Due to the PG-like feature near E_F in $CaRuO_3$ the ω_p values are much smaller than in other transition-metal compounds. The wavelength corresponding to ω_p along *c* (5323 cm^{-1}) is somewhat larger than that (4115 cm^{-1}) obtained from infrared reflectivity measurement [50]. The discrepancy between experiment and theory can be due to thin films used in the experiments while our results are for a perfect single crystal at low temperature. Moreover, the plasma frequency obtained experimentally is estimated from the free-electron approximation which is not strictly valid for transition-metal compounds.

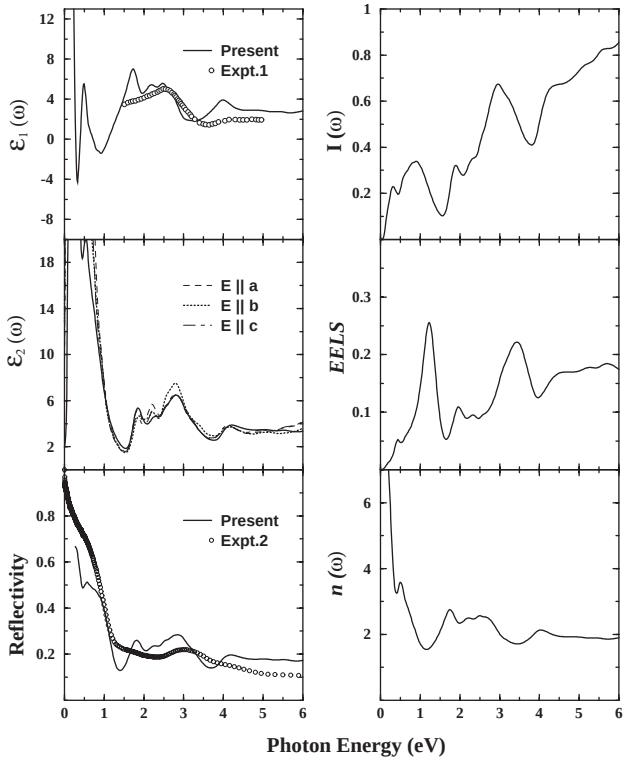

Fig. 8. Linear optical properties for orthorhombic *G*-AF $CaRuO_3$: The left panel shows reflectivity, imaginary [$\varepsilon_2(\omega)$] and real part of optical dielectric tensor [$\varepsilon_1(\omega)$]. The right panel shows refractive index [$n(\omega)$], electron energy loss function (EELS), and absorption coefficient [$I(\omega)$ in 10^5 cm^{-1}]. Experimental data are taken from Ref. [49] (Expt. 1) and Ref. [53] (Expt. 2).

As there should be one-to-one correspondence between band structure and optical spectra, we look first at the imaginary part of the optical dielectric tensor [$\varepsilon_2(\omega)$]. The transitions between the Ru-4*d* states should be forbidden for an isolated atom. However, in $CaRuO_3$, owing to the hybridization between Ru 4*d* and O 2*p* and the local lattice distortions, optical transitions between the Ru-4*d* states are possible [47]. The peak around 1.8 eV (interpreted as on-site Coulomb-repulsion energy) in $\varepsilon_2(\omega)$ is due to such intra-atomic transitions and is in good agreement with the value 1.7 eV obtained from optical measurements [20]. The smaller value of *U* for $CaRuO_3$ compared with that obtained [17] for $LaMnO_3$ (~ 2.22 eV) indicates that the correlation effects for $CaRuO_3$ is of little significance compared with 3*d* transition-metal oxides. A sharp peak in the lower-energy region (<1 eV) in the spectrum originates from intraband transitions facilitated by the metallic nature of $CaRuO_3$. However, in the experimental spectrum [49] for thin films no such peak is found, whereas such a peak-like feature is observed for $SrRuO_3$ films where it is attributed to Drude-like carrier absorption. The fact that no peak is observed for $CaRuO_3$ films is explained [49] by closeness to a metal–insulator boundary. Strain induced substitution of the small Ru^{4+} by the larger Ca^{2+} leads to metal–insulator transition in epitaxial thin films of $CaRuO_3$ [4]. However, as the electronic structure calculations and experimental transport properties [26] predict metallic features for a single crystal of $CaRuO_3$ one should really expect a peak in the experimental single-crystal spectra

at the energy concerned. Consistent with this expectation a recent reflectivity measurement [53] has found such a feature (see the experimental reflectivity spectrum in Fig. 8). The two-peak features at 1.84 and 2.80 eV in the $\varepsilon_2(\omega)$ spectra originate from transitions from Ru $4d(t_{2g})$ to O $2p$ (interband) and from O $2p$ to unoccupied Ca-s and Ru-$4d$ (e_g) states, respectively. In order to check whether optical anisotropy is present in orthorhombic G-AF $CaRuO_3$, we have calculated direction-resolved spectra and show them in the same panel of Fig. 8. Some anisotropy is present in the energy range 2–4 eV, otherwise the spectrum is isotropic in whole energy region shown. We have also calculated the optical properties for the F case, and observed negligible optical anisotropy. The calculated optical $\varepsilon_1(\omega)$ spectrum is compared in Fig. 8 with available experimental data [49]. It is in good agreement with the experimental results in the energy range 1.5–5 eV. Our findings show well-dispersed bands in CB between 2 and 4 eV (Fig. 3), consequently the peaks above 3 eV are not very sharp.

The calculated reflectivity spectrum shows a good correspondence with that experimentally obtained below 5 eV for $CaRuO_3$ thin films [53]. The present calculations of the dielectric function only pertain to the electronic response and do not include the effects of lattice vibrations which dominate the lower-energy part of the spectrum. Consistent with the predicted metallic behavior, $CaRuO_3$ shows a large reflectivity in the lower-energy region. The overall good agreement between the theoretical and experimental optical spectra implies that the present calculations are able to well reproduce the electronic structure of $CaRuO_3$.

The refractive indices for a crystal are closely related to the electronic polarizability of the constituents and the local field inside the crystal. The calculated refractive indices [$n(\omega)$; resembling the real part of the dielectric tensor] for $CaRuO_3$ is shown in the lower-right panel of Fig. 8. The calculated electron energy loss spectrum (EELS; resembling the imaginary part of the dielectric tensor) in Fig. 8 shows peaks at 1.2 and 3.3 eV correspond to the screened plasma frequencies. The calculated absorption coefficient [$I(\omega)$] is shown in the top-right panel. No experimental data for these optical characteristics are available.

4.2. UPS, XPS, and XANES

The fully relativistic angle-resolved intensity of the spectrum is obtained as a product of partial, angular-momentum-dependent cross-sections and partial DOS. The relativistic cross-sections are calculated using the muffin-tin part of the potential over the energy range of the DOS functions for the fixed incident-photon energy. This has been evaluated for the potentials and DOS functions from the self-consistent fully-relativistic full-potential LMTO calculations. However, for the sake of brevity we have not presented the details of the elaborate theoretical method used and refer instead to Ref. [17] for a description. To be consistent with the reported photoemission spectra (PES), we have made all calculations with a fixed incident photon energy of 21.2 eV (corresponding to He(I) source) for UPS and 1486.6 eV (corresponding to Al$K\alpha$ source) for X-ray photoemission spectra (XPS). The calculated spectra enable us to compare our band-structure findings with the available experimental results. Moreover, the origin of the experimentally observed peaks can be determined by site-resolved PES. From the upper panel of Fig. 9, it is seen that our calculated spectrum correctly reproduces the experimental spectra [51,52] in the energy region -6 to 0 eV. In both theoretical and experimental spectra E_F is fixed at 0 eV. A small shoulder-like peak closer to E_F (at $\sim$1.6 eV) is due to the presence of the O(1)-2s and Ru-4d electrons. The strongest peak near -4 eV (which is observed in both experimental studies) has main contributions from O(1) electrons at the apex of the octahedron. From the partial DOS analysis we have already seen that although O(1) and O(2) fall in the

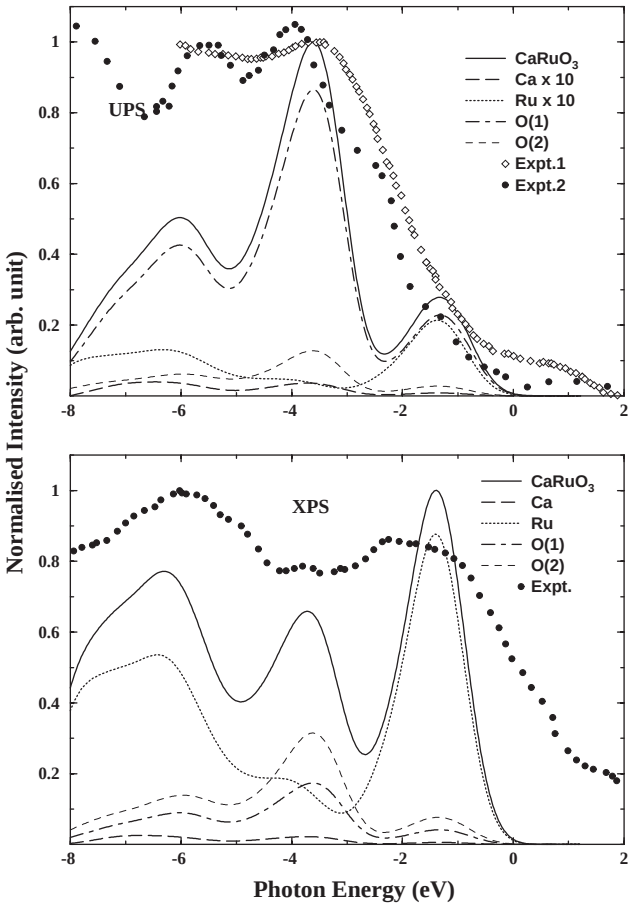

Fig. 9. Calculated UPS and XPS spectra for orthorhombic G-AF $CaRuO_3$. The experimental UPS data (Expt. 1 and 2) are taken from Refs. [51,52], respectively. The experimental XPS data are taken from Ref. [51].

same energy region, they exhibit notable differences. It should further be emphasized that O(2) contributes very little to the peak under consideration. Since Ca^{2+} does not have a considerable number of electrons in VB, its contribution to the spectra in the whole energy range is negligible.

The valleys around −5 eV in the calculated UPS is absent in both experimental spectra due to the following fact. Experimental UPS usually include contributions from inelastically scattered secondary electrons at lower energies which are not taken into account in the theoretical spectrum. Consistent with this viewpoint Cox et al. [52] found a strong peak-like feature at −8 eV which is attributed to the inelastically scattered secondary electrons.

The calculated XPS is shown in the lower panel of Fig. 9 which shows that the peak features in the calculated spectrum agrees extremely well with the experimental spectrum [51] over the entire energy range. As mentioned above, the intensity of the peaks depends upon the partial DOS as well as cross-sections of the constituents of the compound. The first peak around −6 eV is mainly contributed by Ru-4*d* (e_g-like) electrons. The second peak at −4 eV reflects the combined contributions of the O-2*p* and Ru-4*d* electrons. The prominent peak at ~ -1 eV is due to narrow Ru-4*d* (t_{2g}-like) electrons which are also responsible for the magnetism of this material. As the UPS and XPS give information about electronic distribution in VB only, the intensity contributions above E_F in the experimental spectra have no physical meaning and hence this aspect is not commented here.

The calculated O *K*- and Ru *K*-edge XANES for orthorhombic $CaRuO_3$ is shown in Fig. 10. The theoretical O *K*-edge XANES is found to be in good agreement with the experimental spectra in the lower-energy region. No experimental Ru *K*-edge XANES is available for comparison.

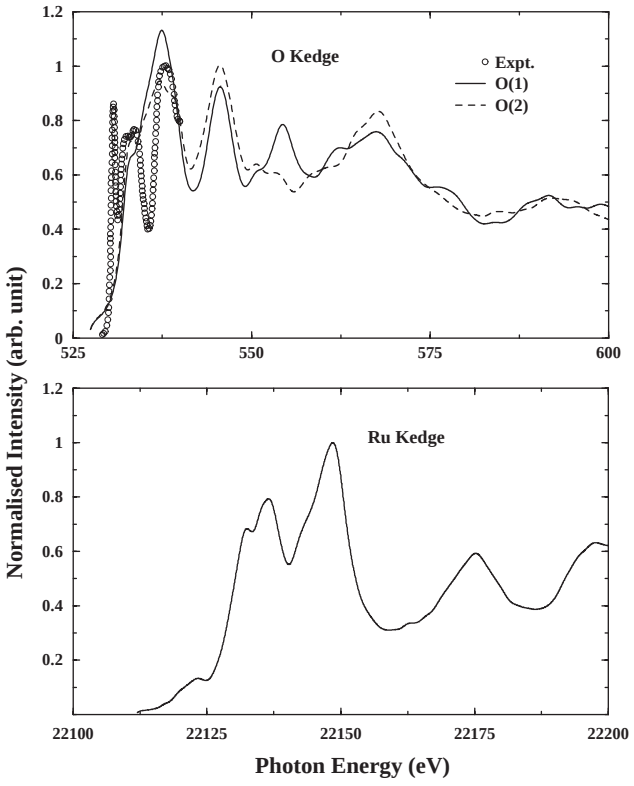

Fig. 10. Calculated XANES spectra for orthorhombic *G*-AF $CaRuO_3$. The experimental O *K*-edge spectrum is taken from Ref. [20].

5. Conclusions

In order to settle the controversy about the magnetic ground state of $CaRuO_3$, we have carried out generalized-gradient-corrected fully-relativistic full-potential calculations for $Sr_{1-x}Ca_xRuO_3$ ($x = 0$, 0.25, 0.5, 0.75, and 1) in P, F, and *A*-, *C*-, and *G*-AF magnetic configurations for the experimentally observed orthorhombic as well as a hypothetical cubic (perovskite aristotype) $CaRuO_3$ and summarized our results as follows.

1. Among the five different magnetic configurations, the orthorhombic *G*-AF phase is found to have the lowest total energy and highest Ru magnetic moment. However, as low-temperature powder neutron diffraction examination has not shown any magnetic peaks, we conclude that $CaRuO_3$ is in a spin-glass state with dominant short-range antiferromagnetic interactions.

2. Owing to the relatively small size of Ca^{2+} the RuO_6 octahedra are tilted which in turn lead to weak hybridization between the Ru-4*d* and O-2*p* electrons resulting in AF ordering. The *G*-AF type exchange interaction produces a pseudogap-like feature in close vicinity of E_F for orthorhombic $CaRuO_3$ which gives extra contribution to stability in this system.

3. The cubic $CaRuO_3$ phase would be stabilized in the F state and the total energies for different magnetic configurations of the cubic phase are much higher than those of the corresponding orthorhombic phases implying that orthorhombic phase is the ground state.

4. The total-energy and magnetic-property studies for $Sr_{1-x}Ca_xRuO_3$ show that this solid-solution phase obeys Goodenough's supposition that magnetic compounds stabilize in the state with the highest magnetic moment.

5. Ru in $CaRuO_3$ are not in the low-spin state. The relatively low magnetic moment of $CaRuO_3$ is due to the small exchange splitting resulting from the extended nature of the 4*d* orbitals.

6. The electronic structure study shows that $CaRuO_3$ is metallic in agreement with experimental findings.

7. The orbital-projected DOS shows that the t_{2g} electrons mainly contribute to the magnetic and transport properties of $CaRuO_3$.

8. The calculated optical properties of orthorhombic *G*-AF $CaRuO_3$ are found to be in good agreement with available experimental spectra. Our theoretically calculated spectral data for orthorhombic *G*-AF and F $CaRuO_3$ are found to be nearly isotropic.

9. The calculated ultra-violet photoemission and X-ray photoemission spectra are in good agreement with experimental spectra in the energy range considered. The same applies to the O *K*-edge X-ray absorption spectrum (the Ru *K*-edge spectrum has also been calculated, but no experimental data are available for comparison).

Acknowledgments

The authors wish to acknowledge Dr. John Wills, Professor K. Schwarz, and Professor Peter Blaha for providing the programs used in this study, and Dr. A. Delin, Dr. H.W. Brinks, and Dr. O.H. Hansteen for useful communications. The authors are grateful for the financial support from the Research Council of Norway. Part of these calculations were carried out on the Norwegian supercomputer facilities.

References

[1] P.R. Van Loan, Am. Ceram. Soc. Bull. 51 (1972) 231.
[2] T. Takeda, R. Kanno, Y. Kawamoto, Y. Takeda, O. Yamamoto, J. Electrochem. Soc. 147 (2000) 1730.
[3] W. Bensch, H.W. Schwalle, A. Reller, Solid State Ionics 43 (1990) 171.
[4] R.A. Rao, Q. Gan, C.B. Eom, R.J. Cava, Y. Suzuki, J.J. Krajewski, S.C. Gausepohl, M. Lee, Appl. Phys. Lett. 70 (1997) 3035.
[5] K. Char, L. Antognazza, T.H. Geballe, Appl. Phys. Lett. 63 (1993) 2420.
[6] G.L. Catchen, T.M. Rearick, D.G. Schlom, Phys. Rev. B 49 (1994) 318.
[7] N. Higashi, N. Okuda, H. Funakubo, Jpn. J. Appl. Phys. 39 (2000) 2780.
[8] A. Callaghan, C.W. Moeller, R. Ward, Inorg. Chem. 5 (1966) 1572.
[9] J.M. Longo, P.M. Raccah, J.B. Goodenough, J. Appl. Phys. 39 (1968) 1327.
[10] T. Sugiyama, N. Tsuda, J. Phys. Soc. Jpn. 68 (1999) 3980.
[11] T.C. Gibb, R. Greatrex, N.N. Greenwood, P. Kaspi, J. Chem. Soc., Dalton Trans. (1973) 1253.
[12] J.L. Martinez, C. Prieto, J. Rodriguez-Carvajal, A. de Andrés, M. Vallet-Regi, J.M. Gonzaler-Calbet, J. Magn. Magn. Mater. 140–144 (1995) 179.
[13] L. Klein, L. Antognazza, T.H. Geballe, M.R. Beasley, A. Kapitulnik, Phys. Rev. B 60 (1999) 1448.
[14] C.N.R. Rao, in: C.N.R. Rao, B. Raveau (Eds.), Colossal Magnetoresistance, Charge Ordering and Related Properties of Manganese Oxides, World Scientific, Singapore, 1998.
[15] G. Santi, T. Jarlborg, J. Phys: Condens. Matter 9 (1997) 9563.
[16] I.I. Mazin, D.J. Singh, Phys. Rev. B 56 (1997) 2556.
[17] P. Ravindran, A. Kjekshus, H. Fjellvåg, A. Delin, O. Eriksson, Phys. Rev. B 65 (2002) 064445.
[18] P. Ravindran, A. Kjekshus, H. Fjellvåg, unpublished.
[19] J.S. Ahn, J. Bak, H.S. Choi, T.W. Noh, J.E. Han, Y. Bang, J.H. Cho, Q.X. Jia, Phys. Rev. Lett. 82 (1999) 5321.
[20] J.S. Lee, Y.S. Lee, T.W. Noh, K. Char, J. Park, S.-J. Oh, J.-H. Park, C.B. Eom, T. Takeda, R. Kanno, cond-mat/0107375, 2001.
[21] H. Kobayashi, M. Nagata, R. Kanno, Y. Kawamoto, Mater. Res. Bull. 29 (1994) 1271.
[22] J.M. Wills, O. Eriksson, M. Alouani, D.L. Price, in: H. Dreysse (Ed.), Electronic Structure and Physical Properties of Materials, Springer, Berlin, 2000, p. 148;
J.M. Wills, B.R. Cooper, Phys. Rev. B 36 (1987) 3809;
D.L. Price, B.R. Cooper, Phys. Rev. B 39 (1989) 4945.
[23] O.K. Andersen, Phys. Rev. B 12 (1975) 3060.
[24] J.P. Perdew, K. Burke, M. Ernzerhof, Phys. Rev. Lett. 77 (1996) 3865.
[25] I. Felner, I. Nowik, I. Bradaric, M. Gospodinov, Phys. Rev. B 62 (2000) 11332.
[26] G. Cao, S. McCall, M. Shepard, J.E. Crow, R.P. Guertin, Phys. Rev. B 56 (1997) 321.
[27] P. Ravindran, A. Delin, B. Johansson, O. Eriksson, J.M. Wills, Phys. Rev. B 59 (1999) 1776.
[28] P. Blaha, K. Schwarz, J. Luitz, WIEN97, Vienna University of Technology, Vienna, Austria 1997; Improved and updated version of the original copyrighted WIEN code, which was published by P. Blaha, K. Schwarz, P. Sorantin, S.B. Trickey, Comput. Phys. Commun. 59 (1990) 399.
[29] B.C. Hauback, H. Fjellvåg, O. Steinsvoll, K. Johansson, O.T. Buset, J. Jørgensen, J. Neutron Res. 8 (2000) 25.
[30] A.C. Larson, R.B. Von Dreele, General Structure Analysis System (GSAS), LANSCE, MS-H 805, Los Alamos National Laboratory, Los Alamos, NM, USA, 1998.
[31] P. Ravindran, A. Kjekshus, H. Fjellvåg, P. James, L. Nordström, B. Johansson, O. Eriksson, Phys. Rev. B 63 (2001) 144409.
[32] M. Shepard, G. Cao, S. McCall, F. Freibert, J.E. Crow, J. Appl. Phys. 79 (1996) 4821.
[33] T. Kiyama, K. Yoshimura, K. Losige, H. Mitamura, T. Goto, J. Phys. Soc. Jpn. 68 (1999) 3372.
[34] J.J. Hauser, J.V. Waszczak, Phys. Rev. B 30 (1984) 5167.
[35] G. Cao, S. McCall, J. Bolivar, M. Shepard, F. Freibert, P. Henning, J.E. Crow, T. Yuen, Phys. Rev. B 54 (1996) 15144.
[36] G. Cao, F. Freibert, J.E. Crow, J. Appl. Phys. 81 (1998) 3884.
[37] N. Kamegashira, T. Mori, A. Imamura, Y. Hinatsu, J. Alloys Compd. 302 (2000) L6.
[38] D. Chowdhury, Spin Glasses and Other Frustrated Systems, World Scientific, Singapore, 1986, p. 7.
[39] P. Ravindran, R. Vidya, P. Vajeeston, A. Kjekshus, H. Fjellvåg, B.C. Hauback, Solid State Commun. 124 (2002) 293.
[40] J.B. Goodenough, in: J.T. Lopusanski, J.T. Pekalski, J. Przystawa (Eds.), Magnetism in Metals and Metallic Compounds, Plenum, New York, 1976.
[41] F. Boucher, R. Rousseau, Inorg. Chem. 37 (1998) 2351.
[42] R. Dronskowski, P.E. Blöchl, J. Phys. Chem. 97 (1993) 8617.
[43] G. Cao, S. McCall, J.E. Crow, R.P. Guertin, Phys. Rev. Lett. 78 (1997) 1751.
[44] R.J. Bouchard, J.L. Gillson, Mater. Res. Bull. 7 (1972) 873.
[45] Y.S. Lee, J.S. Lee, K.W. Kim, T.W. Noh, J. Yu, E.J. Choi, G. Cao, J.E. Crow, Europhys. Lett. 55 (2001) 280.
[46] P. Ravindran, R. Asokamani, Bull. Mater. Sci. 20 (1997) 613.
[47] J.H. Jung, K.H. Kim, D.J. Eom, T.W. Noh, E.J. Choi, J. Yu, Y.S. Kwon, Y. Chung, Phys. Rev. B 55 (1997) 15489.
[48] D.J. Singh, J. Appl. Phys. 79 (1996) 4818.
[49] H.S. Choi, J. Bak, J.S. Ahn, N.J. Hur, T.W. Noh, J. Korean Phys. Soc. 33 (1998) 185.
[50] F.P. de la Cruz, N.E. Massa, V.M. Nassif, S.L. Cuffini, R.E. Carbonio, H. Salva, Phys. Stat. Sol. B 220 (2000) 603.
[51] M.V. Rama Rao, V.G. Sathe, D. Sornadurai, B. Panigrahi, T. Shripathi, J. Phys. Chem. Solids 62 (2001) 797.
[52] P.A. Cox, R.G. Egdell, J.B. Goodenough, A. Hamnett, C.C. Naish, J. Phys. C: Solid State Phys. 16 (1983) 6221.
[53] J.S. Lee, T.W. Noh, Private communication.